Light-induced translation symmetry breaking via nonlinear phononics

Adrián Gómez Pueyo, Alaska Subedi

Light-induced translation symmetry breaking via nonlinear phononics

Adrián Gómez Pueyo* and Alaska Subedi†
CPHT, CNRS, Ecole Polytechnique, IP Paris, F-91128 Palaiseau, France
(Dated: August 11, 2022)

Light has a wavelength that is usually longer than the size of the unit cell of crystals. Hence, even intense light pulses are not expected to break the translation symmetry of materials. However, certain materials, including $KTaO_3$, exhibit peaks in their Raman spectra corresponding to their Brillouin zone boundary phonons due to second-order Raman processes, which provide a mechanism to drive these phonons using intense midinfrared lasers. We investigated the possibility of breaking the translation symmetry of $KTaO_3$ by driving its highest-frequency transverse optic mode $Q_{\rm HX}$ at the X $(0, \frac{1}{2}, 0)$ point. Our first principles calculations show that the energy curve of the transverse acoustic mode $Q_{\rm LZ}$ at X softens and develops a double-well shape as the value of the $Q_{\rm HX}$ coordinate is increased, while that of the other transverse acoustic component $Q_{\rm LX}$ hardens when the value of the $Q_{\rm HX}$ coordinate is similarly varied. We performed similar total energy calculations as a function of the $Q_{\rm HX}$ coordinate and electric field to extract the nonlinear coupling between them. These were then used to construct the coupled equations of motion for the three phonon coordinates in the presence of an external pump term on the $Q_{\rm HX}$ mode, which we numerically solved for a range of pump frequencies and amplitudes. We find that 465 MV/cm is the smallest pump amplitude that leads to an oscillation of the $Q_{\rm LZ}$ mode at a displaced position, hence, breaking the translation symmetry of the material. Such highly intense light pulses cannot be generate by currently available laser sources, and they have the possibility to damage the material. Nevertheless, our work shows that light can in principle be used to break the translation symmetry of a material via nonlinear phononics.

I. INTRODUCTION

Ultrafast structural control of materials by coherently exciting their phonons using intense laser pulses is an active area of research [1–3]. This field of nonlinear phononics started when Först *et al.* realized that a $Q_{\rm S}Q_{\rm IR}^2$ nonlinear coupling between fully-symmetric Raman $Q_{\rm S}$ and infrared $Q_{\rm IR}$ phonon modes can cause a displacement of the lattice along the $Q_{\rm S}$ coordinate when the $Q_{\rm IR}$ mode is externally pumped [4]. A limitation of this type of coupling is the inability to break any crystal symmetry of a material. Nevertheless, an investigation of this nonlinearity in perovskite ferroelectrics using first principles calculations has found that this mechanism can be used to switch their electrical polarization [5], and this theoretical prediction has been partially confirmed in subsequent experiments [6, 7].

Historically, only cubic nonlinearities between Raman and infrared phonons were investigated in the context of ionic Raman scattering [8, 9]. However, first principles calculations in Ref. [10] showed that a symmetry-breaking Raman phonon mode $Q_{\rm R}$ can have substantial quartic-order $Q_{\rm R}^2Q_{\rm IR}^2$ coupling with an infrared phonon mode. Such a large quartic-order coupling between two infrared modes has also been calculated in oxide paraelectrics, which has been used to predict light-induced ferroelectricity [11]. Radaelli has shown that driving degenerate infrared modes along orthogonal directions can cause displacement of the lattice along a symmetry-breaking Raman mode due to a cubic-order nonlinearity [12], while a separate study has shown that the symmetry-breaking Raman mode oscillates about the equilibrium position with the difference frequency when nondegenerate infrared phonons are driven along orthogonal directions [13]. Additional theoretical and experimental studies have demonstrated that nonlinear phononics is a useful technique to control the crystal structure and, hence, the physical properties of materials [14–32]. However, these studies have only focused on light-induced structural modifications that do not change the size of the unit cell thus far.

In this paper, we investigate the possibility of breaking the translation symmetry of $KTaO_3$ using light by driving its Brillouin zone boundary phonon modes. This was motivated by the observation of large two-phonon peaks due to zone boundary modes in the Raman spectrum of this material [33], indicating that these modes couple significantly to light. We obtained the nonlinear couplings between the highest-frequency transverse optic (TO) mode $Q_{\rm HX}$ and doubly-degenerate components of the transverse acoustic (TA) mode $Q_{\rm LZ}$ and $Q_{\rm LX}$ at the X $(0, \frac{1}{2}, 0)$ point using first principles total-energy calculations, which show that the TA $Q_{\rm LZ}$ mode softens when the orthogonal TO coordinate $Q_{\rm HX}$ has a finite value. The coupling between the $Q_{\rm HX}$ mode and electric field was obtained from similar total energy calculations. These were then used to construct coupled equations of motion for the phonon coordinates. Their numerical solutions showed that the TA $Q_{\rm LZ}$ mode can rectify and break the translation symmetry of the lattice when the $Q_{\rm HX}$ mode is pumped. However, 465 MV/cm is the lowest pump amplitude that causes the rectification. Beyond the possibility of sample damage by such an intense pulse,

* adrian.gomez@polytechnique.edu
† alaska.subedi@polytechnique.edu

the required intensity is also at least an order of magnitude larger than that can be produced by currently available midinfrared laser sources. Nevertheless, our study demonstrates that light can in principle be used to break the translation symmetry of crystals through nonlinear phononics and motivates search for materials that exhibit large two-phonon Raman peaks due zone-boundary modes.

II. THEORETICAL APPROACH

We used the theoretical approach outlined in Ref. [10] to study the dynamics of the doubly-degenerate TA modes of $KTaO_3$ at the X point when its highest-frequency TO mode at X is externally pumped through second-order Raman process. This density functional theory based first-principles approach requires the calculation of the phonon eigenvectors, which are then used to calculate the total energy surface $V(Q_{\rm HX}, Q_{\rm LX}, Q_{\rm LZ})$ as a function of the high-frequency optical and low-frequency acoustic modes. The total energy surface is fit with a polynomial to extract the phonon anharmonicities and phonon-phonon nonlinear couplings (the full expression can be found in Appendix A), and these are used to construct the coupled equations of motion for the phonon coordinates. The coupling between the pumped mode and light is extracted by calculating the total energy as a function of the $Q_{\rm HX}$ mode and electric field, an approach previously used by Cartella *et al.* [34]. The coupled equations of motion are solved numerically in the presence of a pump term for the $Q_{\rm HX}$ mode to obtain the structural evolution of the material as a function of time.

We used QUANTUM ESPRESSO [35] (QE) for the computations of the phonon frequencies and eigenvectors and the total energy surfaces as a function of the phonon coordinates and electric field. These were performed using ultrasoft pseudopotentials with the valence orbitals $3s^2 3p^6 4s^1$ (K), $5s^2 5p^6 5d^3 6s^1$ (Ta) and $2s^2 2p^4$ (O) from the GBRV library [36]. For the exchange and correlation functional, we chose the PBEsol generalized gradient approximation [37]. The plane-wave cutoffs for the basis set and charge density expansions were set to 60 and 600 Ry, respectively. As we are dealing with an insulator with a gap, the electronic occupation was set to fixed.

The first step in our calculations was the relaxation of the unit cell, where we allowed the variation of both the lattice parameter and the atomic positions. We let the relaxation process run until the difference in the total energy between two steps of the self-consistent field (SCF) cycles was less than 10^{-10} Ry, the estimated error of the electronic density (which in our case is calculated as the electrostatic self energy of the difference between the electronic densities at the beginning and the end of each step of the calculation) was below 10^{-11} Ry, and the components of the forces exerted on each atom were smaller than 10^{-6} Ry/Bohr. We used a $12\times12\times12$ Monkhorst-Pack k-point grid for the relaxation process. The lattice parameter obtained was $a = 3.98784$ Å, in good agreement with the experimental value $a_{\rm exp} = 3.988$Å [38].

Once we had the relaxed unit cell, we used it for the computation of the phonon frequencies and eigenvectors at the Brillouin zone boundary point X $(0, \frac{1}{2}, 0)$, which was performed using density functional perturbation theory [39] as implemented in QE. The computation of the dynamical matrix requires a previous SCF calculation which was performed using an $8\times8\times8$ Monkhorst-Pack k-point grid. Then for the dynamical matrix calculation we set a threshold for the self-consistent calculation of 10^{-18} Ry. The diagonalization of the dynamical matrix was realized using the `dynmat` utility in QE, thus obtaining the eigenvectors and frequencies of the different phonons.

For the computation of the phonon anharmonicities and phonon-phonon nonlinear couplings, we used the calculated phonon eigenvectors to create modulated structures as a function of the $Q_{\rm HX}$, $Q_{\rm LX}$, and $Q_{\rm LZ}$ coordinates in $1\times2\times1$ supercells that are required to simulate the phonons at the X point, and then calculated the total energies of these structures. We sampled values of the phonon coordinates ranging from -3.0 to 3.0 Å$\sqrt{\rm u}$. Steps of 0.025 and 0.1 Å$\sqrt{\rm u}$ were used for sampling the total-energy surfaces as a function of two and three coordinates, respectively. A convergence threshold of 10^{-10} Ry for the electronic density in the SCF iterations and an $8\times4\times8$ Monkhorst-Pack k-point grid was used in these calculations. To extract the anharmonicities and nonlinear coupling constants, we fit the calculated total-energy surfaces with polynomials having only the symmetry-allowed nonlinear terms using the GLM [40] package as implemented in JULIA. The extracted coefficients of the polynomials are given in Appendix A.

We used the modern theory of polarization [41] as implemented in QE to calculate the total energy of this material as a function of the $Q_{\rm HX}$ coordinate and electric field E and fit the resulting energy surface to the following expression:

$$H(Q_{\rm HX}, E) = \frac{1}{2}\Omega^2_{\rm HX}Q^2_{\rm HX} + c_4Q^4_{\rm HX} + c_6Q^6_{\rm HX} + c_8Q^8_{\rm HX} + rE + sE^2 + tE^4 + \alpha Q^2_{\rm HX}E^2. \quad (1)$$

Here the frequency $\Omega_{\rm HX}$ and anharmonic coefficients c_i of the $Q_{\rm HX}$ mode are those extracted from the previous total-energy calculations, and $s = -1.4829$ eÅ^2/V, $t = -0.162$ eÅ^4/V^3 and α are the coefficients for the terms allowed by symmetry for the electric field. The linear term for E in $H(Q_{\rm HX}, E)$ with corresponding coupling coefficient $r = -99.696$ eÅ occurs due to the use of periodic boundary condition. We sampled the electric field from -36 to 36 MV/cm with a step of 0.36 MV/cm and $Q_{\rm HX}$ from -3.0 to 3.0 Å$\sqrt{\rm u}$ with a step of 0.3 Å$\sqrt{\rm u}$. For these calculations, we used an $8\times8\times8$ Monkhorst-Pack k-grid. Like in the previous case, the GLM package was used to perform the fit. The polynomial given in Eq. 1 fits the calculated total-energy surface

well, which is consistent with the fact that the form of the coupling between the electric field and phonon at the X point is $\alpha Q_{\rm HX}^2 E^2$ at the lowest order [42]. The fit gives a value for the coupling constant $\alpha = 0.074$ e/(V u). In order to check this method of computing the light-phonon coupling, we also calculated the coupling of the electric field to the highest frequency phonons of $KTaO_3$ at the Γ point, obtaining Born effective mode charge of $Z^{*\rm calc} = 1.03$ e/$\sqrt{\rm u}$, which is in good agreement with the value of $Z^{*\rm pert} = 1.07$ e/$\sqrt{\rm u}$ calculated using density functional perturbation theory [11]. We note that the largest electric field used in the total-energy calculations are more than an order of magnitude smaller than the values that cause rectification of the $Q_{\rm LZ}$ mode in the numerical solution of the equations of motion discussed later. Larger values of the electric field in total-energy calculations caused oscillations in the SCF iterations. This is a limitation of the currently available computational method.

The integration of the differential equations required for the solution of the equations of motion was carried out using the Strong Stability Preserving method of Ruuth, an explicit Runge-Kutta order 3 propagator with 6 stages as implemented in the DifferentialEquations [43] package from the julia language. The time range for the propagation was from 0 to 8 ps, with a time step of 8×10^{-6} ps. The peak amplitude of the laser pulse was set to reach at 4 ps. For the initial conditions, we chose $Q_{\rm HX} = Q_{\rm LX} = Q_{\rm LZ} = 0.1$ Å$\sqrt{\rm u}$, while their first derivatives with respect to time were set to 0. In order to simulate the thermal fluctuations of the phonons, we added a stochastic term in the form of white noise to the equations of motion from the start of the propagation until the pulse reaches its peak. Due to the presence of this term, the solution obtained will depend on the particular string of random values generated for each propagation. The criterion that we followed to determine the outcome of the propagation (in our case, whether or not there is a rectification of the $Q_{\rm LZ}$ mode) was to solve the equations multiple times under the same pump amplitude and frequency conditions, but with a different seed for the random number generator for each run. Then we pick the most probable solution among those obtained, i. e., the one that occurs the most number of times in at the end of our propagations. The Fourier transform of the solutions was obtained using the fftw [44] package as implemented in julia.

III. RESULTS AND DISCUSSION

The TA and TO modes of $KTaO_3$ at X are doubly degenerate. The TA mode is the lowest-frequency phonon at X, whereas there are four TO phonon branches in this material. Figs. 1(top) and (bottom) show the atomic displacements corresponding to the $Q_{\rm LZ}$ and $Q_{\rm HX}$ components of the TA and highest-frequency TO modes, respectively. The calculated frequencies of these modes are $\Omega_{\rm LZ}$ = 61 cm^{-1} and $\Omega_{\rm HX}$ = 509 cm^{-1}, respectively. These are in good accord with the values inferred from the Raman experiments of Nilsen and Skinner, where these modes manifest as peaks at 123 and 1095 cm^{-1} corresponding to the doubling of the respective phonon frequencies due to second-order Raman processes [33]. Both these modes belong to the irreducible representation X_5^+ of the cubic structure with the space group $Pm\bar{3}m$. The $Q_{\rm LZ}$ mode involves displacement of the Ta ions against the O octahedra along the z direction. The $Q_{\rm HX}$ mode causes one set of planar O ions to move against the Ta ions in the x direction, while another set of planar O ions remain stationary. This mode also displaces the apical O ions along the x direction against the movement of the planar O ions. Since these modes have the wavevector $(0, \frac{1}{2}, 0)$, the atomic displacements within the adjacent unit cells are out-of-phase along the y direction, thus breaking the translation symmetry. The distorted structure has the orthorhombic space group $Pmma$.

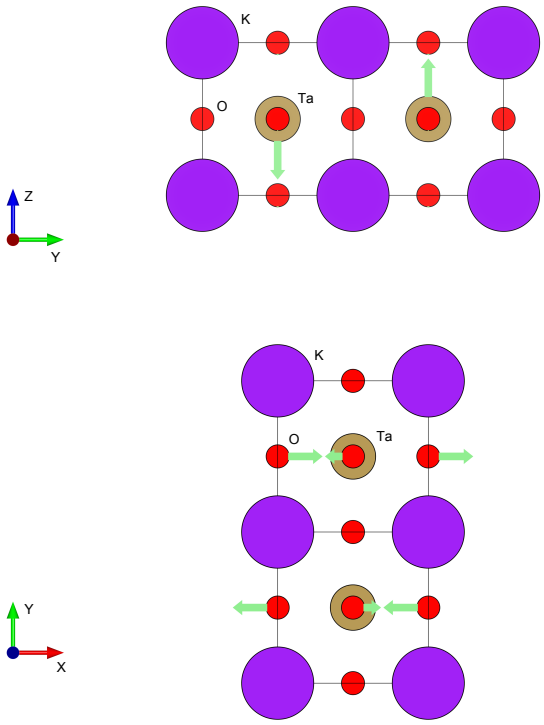

FIG. 1. Schematic representations of the phonon modes of $KTaO_3$ at the X $(0, 1/2, 0)$ point considered in the present work. (Top) The TA mode component $Q_{\rm LZ}$ that has atomic movements polarized along the z direction. The other degenerate component of this mode $Q_{\rm LX}$ has the same atomic movements but are directed along the x axis. The TA mode is the lowest-frequency mode at X in $KTaO_3$. (Bottom) The highest-frequency TO mode $Q_{\rm HX}$ that has atomic movements polarized along the x direction.

We calculated the total energy as a function of the $Q_{\rm HX}$

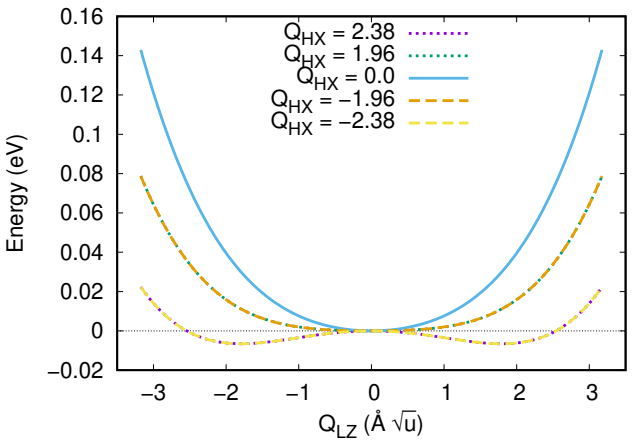

FIG. 2. Total energy as a function of the Q_{LZ} phonon coordinate for different values of the Q_{HX} phonon coordinate. For visual clarity, the zero energy point has been chosen so that the curves coincide at $Q_{\mathrm{LZ}} = 0$.

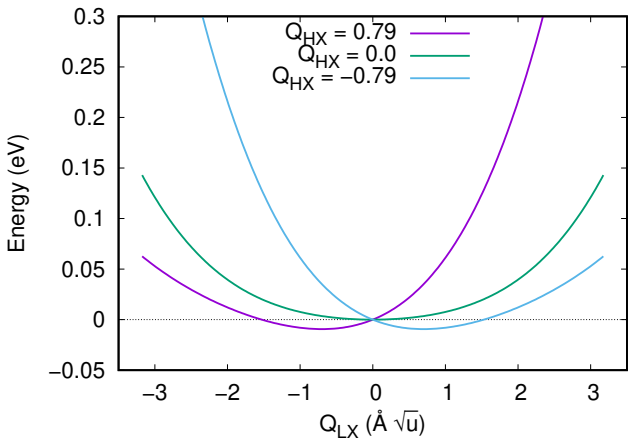

FIG. 3. Total energy as a function of the Q_{LX} phonon coordinate for different values of the Q_{HX} phonon coordinate. For visual clarity, the zero energy point has been chosen so that the curves coincide at $Q_{\mathrm{LX}} = 0$.

and Q_{LZ} coordinates, and Fig. 2 shows five energy curves from this energy surface $V(Q_{\mathrm{HX}}, Q_{\mathrm{LX}} = 0, Q_{\mathrm{LZ}})$. We can see that the total energy as a function of the Q_{LZ} coordinate for a fixed value of the Q_{HX} coordinate is symmetric upon the transformation $Q_{\mathrm{LZ}} \to -Q_{\mathrm{LZ}}$. The Q_{HX} and $-Q_{\mathrm{HX}}$ energy curves also overlap with each other. This implies that the energy surface is an even function of both Q_{LZ} and Q_{HX}, and these coordinates occur only with even powers in the polynomial fit of the energy surface. This is consistent with the symmetry requirement that the coupling terms occur with even powers of the coordinates when they are orthogonal to each other.

The energy curve of the Q_{LZ} coordinate softens when the Q_{HX} coordinate has a finite value, and it develops a double-well shape at large values of the Q_{HX} coordinate. This is reflected in the negative sign of the coefficients in the nonlinear coupling terms $g_1 Q_{\mathrm{HX}}^2 Q_{\mathrm{LZ}}^2$, $g_2 Q_{\mathrm{HX}}^4 Q_{\mathrm{LZ}}^2$, and $g_3 Q_{\mathrm{HX}}^2 Q_{\mathrm{LZ}}^4$ in the fit of $V(Q_{\mathrm{HX}}, Q_{\mathrm{LX}} = 0, Q_{\mathrm{LZ}})$ (see Appendix A). The total force experienced along the Q_{LZ} coordinate is given by $-\partial V/\partial Q_{LZ}$, and the effect of the nonlinear terms is to renormalize its frequency as $\Omega_{\mathrm{LZ}}^2 \to \Omega_{\mathrm{LZ}}^2(1 + 2g_1 Q_{\mathrm{HX}}^2 + 2g_2 Q_{\mathrm{HX}}^4 + 4g_3 Q_{\mathrm{HX}}^2 Q_{\mathrm{LZ}}^2 + \cdots)$. Since the phonon coordinates Q_{HX} and Q_{LZ} appear with even powers in this expression, their contribution to the renormalization will not be averaged out over time. As a result, the low-frequency mode Q_{LZ} softens when the high-frequency mode Q_{HX} is oscillating with a finite amplitude.

We also investigated the dynamics along the Q_{LX} component of the TA mode that has atomic displacements parallel to that of the high-frequency Q_{HX} mode. The energy curves of the Q_{LX} coordinate for several values of the Q_{HX} coordinate extracted from the calculated total-energy surface $V(Q_{\mathrm{HX}}, Q_{\mathrm{LX}}, Q_{\mathrm{LZ}} = 0)$ is shown in Fig. 3. In this case we can see that the minimum of the Q_{LX} coordinate shifts when the Q_{HX} coordinate has a finite value, and the direction of this displacement depends on the sign of Q_{HX}. The curves with the same magnitude of Q_{HX} but opposite sign are mirror images of each other, with the mirror plane located at $Q_{\mathrm{LX}} = 0$. In addition, the energy curves of the Q_{LX} mode noticeably harden as the magnitude of the Q_{HX} coordinate is increased, which contrasts with the softening exhibited by Q_{LZ} mode. This implies that the energy surface includes terms of the form $Q_{\mathrm{HX}}^i Q_{\mathrm{LX}}^j$ with both even and odd powers, subject to the condition $i + j = 2n$, where n is an integer. Once again, this is in accord with the symmetry requirements for two modes with the same irreducible representation and parallel polarization.

We constructed the coupled equations of motion for the Q_{HX}, Q_{LX}, and Q_{LZ} coordinates using the calculated total-energy surfaces as the potential energy. These equations read

$$\begin{aligned}
\ddot{Q}_{\mathrm{HX}} + \gamma_{\mathrm{HX}}\dot{Q}_{\mathrm{HX}} + \Omega_{\mathrm{HX}}^2 Q_{\mathrm{HX}} &= -\frac{\partial V^{\mathrm{nh}}(Q_{\mathrm{HX}}, Q_{\mathrm{LX}}, Q_{\mathrm{LZ}})}{\partial Q_{\mathrm{HX}}} \\
&\quad + F(t), \\
\ddot{Q}_{\mathrm{LX}} + \gamma_{\mathrm{LX}}\dot{Q}_{\mathrm{LX}} + \Omega_{\mathrm{LX}}^2 Q_{\mathrm{LX}} &= -\frac{\partial V^{\mathrm{nh}}(Q_{\mathrm{HX}}, Q_{\mathrm{LX}}, Q_{\mathrm{LX}})}{\partial Q_{\mathrm{LX}}}, \\
\ddot{Q}_{\mathrm{LZ}} + \gamma_{\mathrm{LZ}}\dot{Q}_{\mathrm{LZ}} + \Omega_{\mathrm{LZ}}^2 Q_{\mathrm{LZ}} &= -\frac{\partial V^{\mathrm{nh}}(Q_{\mathrm{HX}}, Q_{\mathrm{LX}}, Q_{\mathrm{LZ}})}{\partial Q_{\mathrm{LZ}}}.
\end{aligned} \tag{2}$$

Here $V^{\mathrm{nh}}(Q_{\mathrm{HX}}, Q_{\mathrm{LX}}, Q_{\mathrm{LZ}})$ is the nonharmonic part of the polynomial fit to the calculated total-energy surfaces as a function of the three coordinates and γ_i's are the damping coefficients of the corresponding normal modes, which we set to 10% of the value of their corresponding natural frequency. The full polynomial expression of V^{nh} with terms up to the eight order that was used for fitting the calculated total-energy surfaces is given in Appendix A.

$F(t)$ is the external force experienced by the $Q_{\rm HX}$ coordinate due to the pump pulse. This was taken into account by considering the force on $Q_{\rm HX}$ due to an electric field, which is given by

$$\begin{aligned} F &= -\frac{\partial H(Q_{\rm HX}, E)}{\partial Q_{\rm HX}} \\ &= -2\alpha Q_{\rm HX} E^2. \end{aligned} \tag{3}$$

We studied the dynamics using Gaussian-enveloped single-frequency pulses

$$E_{\rm sf}(t) = E_0 \sin(\omega t) e^{-t^2/2(\sigma/2\sqrt{2\log 2})^2}. \tag{4}$$

Here, E_0 is the amplitude of the pulse and ω its frequency. The pulse has a Gaussian envelope with full-width at half maximum of σ.

The coupled equations of motion for the $Q_{\rm HX}$, $Q_{\rm LX}$, and $Q_{\rm LZ}$ coordinates given in Eq. 2 were solved for different values of pump amplitude E_0 and frequency ω. For small values of the pump amplitude E_0, the energy transferred to $Q_{\rm HX}$ by the external pulse is small. This mode then oscillates at its natural frequency $\Omega_{\rm HX}$ without getting amplified regardless of the frequency of the pump pulse and decays at a rate determined by $\gamma_{\rm HX}$. As a result, the force imparted on the $Q_{\rm LZ}$ and $Q_{\rm LX}$ coordinates due to the oscillation of $Q_{\rm HX}$ is also small, and $Q_{\rm LZ}$ and $Q_{\rm LX}$ also exhibit decaying oscillations about their natural frequency $\Omega_{\rm LX} = \Omega_{\rm LZ}$. For very large values of pump amplitude E_0, all three modes diverge, which describes the breakdown of the material at very high electric field of the pump. In between these two limiting behaviors, we searched for a range of pump frequency and amplitude that causes the $Q_{\rm LZ}$ mode to oscillate at a displaced position.

We find that $\omega = 1.8\Omega_{\rm HX}$ is the lowest pump frequency that leads to a rectification of the $Q_{\rm LZ}$ coordinate, which occurs for a pump amplitude of 465 MV/cm. The solutions of the equations of motion for the $Q_{\rm HX}$, $Q_{\rm LX}$ and $Q_{\rm LZ}$ coordinates for these values of pump frequency and amplitude are shown in Fig. 4. As one can see, the low-frequency $Q_{\rm LZ}$ coordinate oscillates at a displaced position while the externally-pumped $Q_{\rm HX}$ coordinate is oscillating with a large amplitude. This implies that the translation symmetry of the lattice is broken because the $Q_{\rm LZ}$ coordinate has a non-zero average value within this duration. When the $Q_{\rm HX}$ mode decays after the diminution of the pump pulse, the $Q_{\rm LZ}$ coordinate goes back to oscillating about the equilibrium position with a decaying amplitude. In the Fourier transform of $Q_{\rm LZ}(t)$, the displaced motion appears as a large intensity around zero frequency, while the amplified oscillations after the pump appear as a peak near the original frequency $\Omega_{\rm LZ}$.

Fig. 4 also shows that the externally-pumped phonon mode $Q_{\rm HX}$ is highly amplified and oscillates with an amplitude of $\sim$3 Å$\sqrt{\rm u}$. Its Fourier transform shows a resonance peak at the frequency of the pump pulse in this regime, but frequency components between $\Omega_{\rm HX}$ to $\sim 2.5\Omega_{\rm HX}$ also show significant contribution. This reflects the parametrically-driven nature of the equation of motion of the $Q_{\rm HX}$ mode because the external force $F(t) = -2\alpha Q_{\rm HX} E(t)^2$ due to the pump pulse is linear in $Q_{\rm HX}$. As a result, the frequency of the driven $Q_{\rm HX}$ mode varies with time and acquires components that are not resonant with respect to the harmonic frequency of the mode or the pump frequency. The other TA coordinate $Q_{\rm LX}$ with atomic motions parallel to the $Q_{\rm HX}$ mode, whose dynamics is also shown in the figure, is moderately amplified while the $Q_{\rm HX}$ mode is making large-amplitude oscillations. Fourier transform of the time evolution of this mode shows a large peak at the pump frequency. This high-frequency oscillation of the TA $Q_{\rm LX}$ mode reflects the large $Q_{\rm HX}^2 Q_{\rm LX}^2$ nonlinearity.

At a pump frequency of $\omega = 1.8\Omega_{\rm HX}$, the $Q_{\rm LZ}$ coordinate makes only a single cycle of oscillation at a displaced position during the pump pulse. This indicates that the effective double-well potential experienced by this mode is shallow. Indeed, we find that the range of pump amplitude that causes the rectification of the $Q_{\rm LZ}$ mode is relatively narrow for this value of pump frequency. The $Q_{\rm LZ}$ coordinate again oscillates about the equilibrium position as the pump amplitude is increased above 525 MV/cm. However, the amplitude of oscillations remain larger than 3 Å$\sqrt{\rm u}$, indicating that $Q_{\rm LZ}$ mode oscillates across the minima of the double-well potential at these higher values of pump amplitude.

Fig. 5 shows the ranges of pump amplitudes that rectify the $Q_{\rm LZ}$ coordinate when the $Q_{\rm HX}$ coordinate is pumped at frequencies between $1.7\Omega_{\rm HX}$ and $2.5\Omega_{\rm HX}$ and amplitudes between 400 and 700 MV/cm. We actually solved the equations of motion of the phonon coordinates for pump frequencies up to $3.0\Omega_{\rm HX}$ and amplitudes up to 1500 MV/cm. As already mentioned, the equations of motion include a white noise term to simulate the thermal fluctuations of the phonons. Up to a pump amplitude of 700 MV/cm, the presence (or absence) of rectification of the $Q_{\rm LZ}$ mode is independent of the noise term with the exception of the values of pump amplitude and frequency near the border between rectification and no rectification, where both outcomes appear in the solutions of the equations of motion. Larger pump values cause the appearance of divergences in the solution that pervade the entirety of the range of frequencies studied, and we enter a new regime of the dynamics of the system that we will analyze below. For this reason Fig. 5 is limited to the values of pump amplitude and frequency that induce rectification without possible breakdown of the material.

We can see that the value of the smallest pump amplitude that rectifies the $Q_{\rm LZ}$ coordinate increases with the pump frequency. It is 465 MV/cm for $\omega = 1.8\Omega_{\rm HX}$ and increases to 675 MV/cm for $\omega = 2.5\Omega_{\rm HX}$. This increasing dependence derives from the fact that a larger pump amplitude is required to resonantly excite the $Q_{\rm HX}$ coordinate at higher pump frequencies. The largest pump amplitude that rectifies the $Q_{\rm LZ}$ coordinate increases steeply as a function of the pump frequency. It is 520 MV/cm

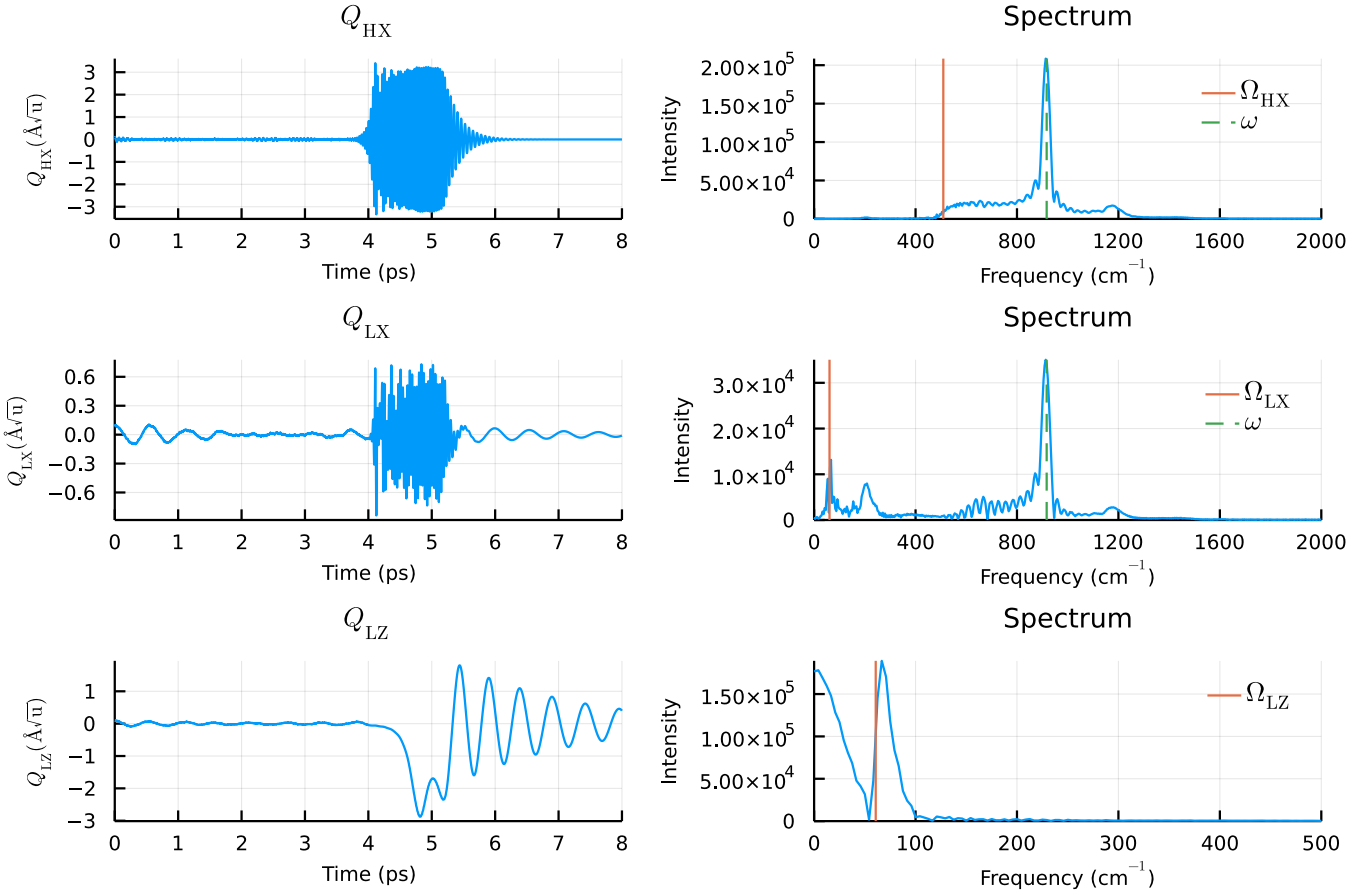

FIG. 4. (Left) Dynamics of the (top) TO $Q_{\rm HX}$, (middle) TA $Q_{\rm LX}$, and (bottom) TA $Q_{\rm LZ}$ phonon coordinates at the X point for a single-frequency pump pulse with amplitude $E_0 = 465$ MV/cm and frequency $\omega = 1.8\Omega_{\rm HX}$. (Right) Fourier transform of the time evolution of the respective coordinates. The solid vertical lines mark the natural frequencies of each mode, while the dashed one indicates the frequency of the pump pulse.

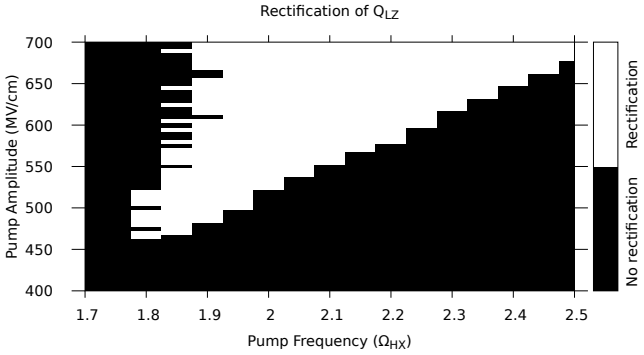

FIG. 5. Values for the amplitude and frequency of the single-frequency pulse used to pump the $Q_{\rm HX}$ phonon coordinate that induce rectification of the $Q_{\rm LZ}$ coordinate.

for $\omega = 1.8\Omega_{\rm HX}$ and increases to a value of more than 700 MV/cm for $\omega = 1.9\Omega_{\rm HX}$, where the solutions become dependent on noise as discussed in the previous paragraph. In fact the rectified solutions for the $Q_{\rm LZ}$ coordinate appear at pump amplitudes up to 840, 1410, and 1490 MV/cm for $\omega = 1.9\Omega_{\rm HX}$, $2.1\Omega_{\rm HX}$, and $2.5\Omega_{\rm HX}$, respectively. At higher pump frequencies, the largest pump amplitude that gives a rectified solution flatlines at 1490 MV/cm up till the largest pump frequency of $3.0\Omega_{\rm HX}$ that we tested. On the other hand, the lowest pump amplitude that rectifies $Q_{\rm LZ}$ keeps slowly increasing to a value of 840 MV/cm for $\omega = 3.0\Omega_{\rm HX}$. Therefore, the window of pump amplitude that rectifies the $Q_{\rm LZ}$ mode is narrow when rectification starts occurring at $\omega = 1.8\Omega_{\rm HX}$, broadens up to $\omega = 2.5\Omega_{\rm HX}$, and starts narrowing again as the pump frequency is further increased.

We now illustrate the light-induced dynamics for the case of a pump frequency that exhibits a large window of rectification of the $Q_{\rm LZ}$ coordinate as a function of the pump amplitude. The three columns of Fig. 6 show the solutions of the coupled equations of motion of the three phonon coordinates at a pump frequency of $2.3\Omega_{\rm HX}$ for pump amplitudes of 615, 800, and 1100 MV/cm. At 615 MV/cm, which is the lower threshold of the rectification window for this pump frequency, the $Q_{\rm LZ}$ mode exhibits

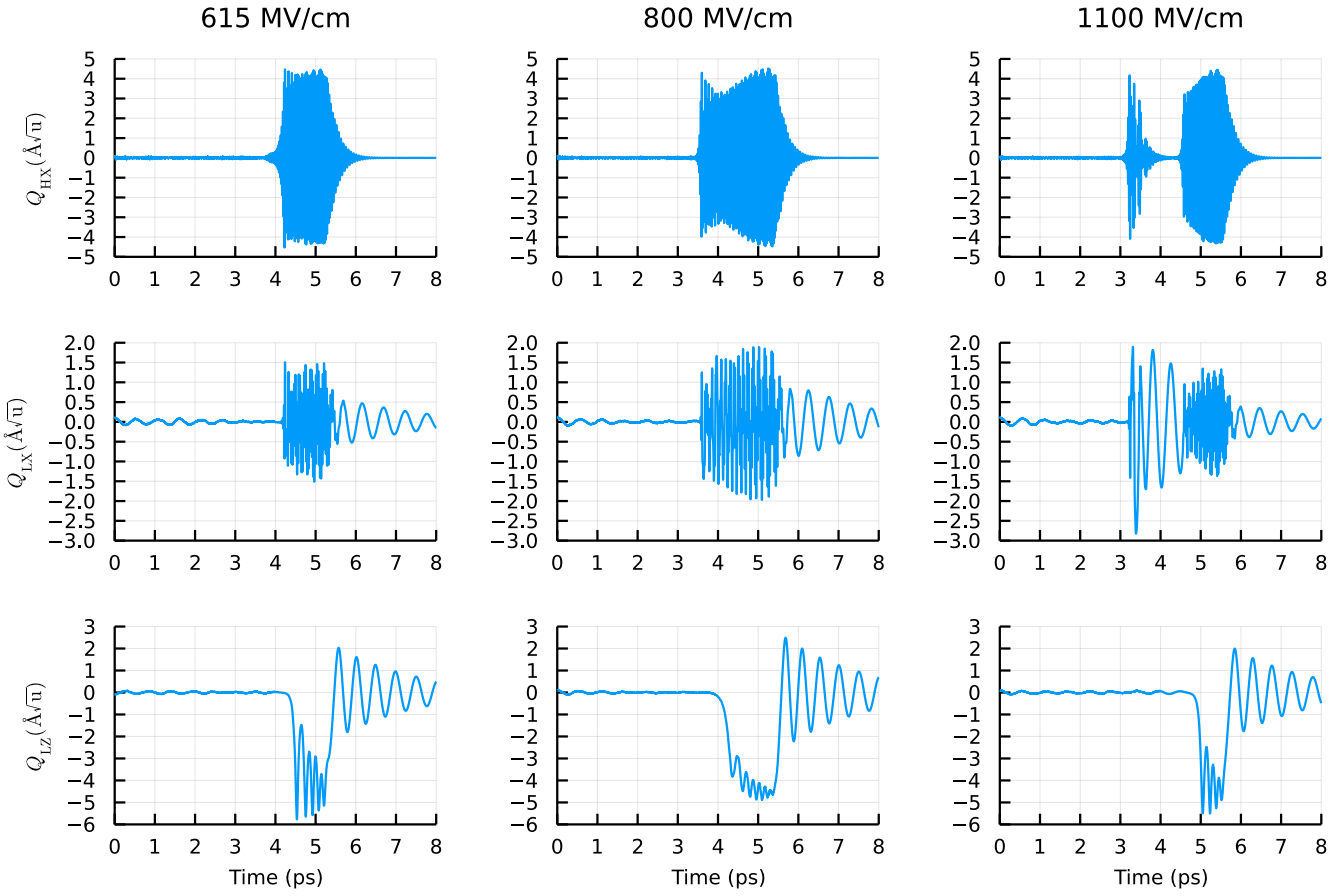

FIG. 6. Dynamics of the $Q_{\rm HX}$, $Q_{\rm LX}$ and $Q_{\rm LZ}$ phonon coordinates for pump pulses with frequency $\omega = 2.3\Omega_{\rm HX}$ and amplitudes of 615, 800 and 1100 MV/cm.

six cycles of oscillations while it is rectified [bottom panel in Fig. 6(left)]. This indicates that the larger value of the pump amplitude required for rectification at a higher pump frequency makes the effective double-well potential deeper, which increases the frequency of the $Q_{\rm LZ}$ mode when it is rectified. Furthermore, the oscillations of the $Q_{\rm LZ}$ mode occur about $\sim$4 Å$\sqrt{\rm u}$, indicating that the minima of the effective double-well potential gets further away from the equilibrium value of zero for a larger value of the pump amplitude.

Fig. 6 (middle) shows the dynamics at an increased pump amplitude of 800 MV/cm while keeping the pump frequency fixed at $2.3\Omega_{\rm HX}$. The $Q_{\rm LZ}$ mode now makes eight cycles while displaced from the equilibrium position. This happens not due to an increase in the frequency of the oscillations in the rectified regime but because the mode gets rectified for a longer duration. There is only a marginal change in the position about which this mode oscillates while it is rectified. Furthermore, the maximum amplitude of the oscillations of the $Q_{\rm LZ}$ mode gets reduced. Interestingly, the amplitude of the oscillation of the pumped $Q_{\rm HX}$ mode also does not increase as the pump amplitude is increased from 615 to 800 MV/cm. Instead, its amplitude as a function of time exhibits a small dip before increasing again by a similar amount. The amplification of the $Q_{\rm HX}$ also occurs for a longer duration. Therefore, the additional pump energy causes rectification and amplification for a longer duration rather than displacing the $Q_{\rm LZ}$ mode to a larger distance or increasing the amplification of the $Q_{\rm HX}$ mode. The additional pump energy also flows to the $Q_{\rm LX}$ mode, whose amplified oscillations last for a longer duration as well.

Fig. 6 (right) shows the dynamics when the pump amplitude is further increased to 1100 MV/cm while keeping the pump frequency at $2.3\Omega_{\rm HX}$. The amplified oscillations of the pumped $Q_{\rm HX}$ mode now splits into two different packets that are separated by a region where the mode is unamplified. The $Q_{\rm LZ}$ mode gets rectified, but only during the amplified oscillations of the $Q_{\rm HX}$ mode in the packet of the later time delay. As a result, the $Q_{\rm LZ}$ mode makes only four cycles of oscillations at a displaced position. Neither the amount of displacement from the equilibrium position nor the amplitude of oscillations of the $Q_{\rm LZ}$ mode increase in the rectified regime at this increased value of the pump amplitude. The amplitude of the $Q_{\rm HX}$ mode also does not increase, while this mode in fact now makes amplified oscillations for a shorter

duration. However, the Q_{LX} mode now oscillates with a much larger amplitude during the initial part of the pump pulse, and this accounts for the additional energy pumped into the system.

At higher pump frequencies, we find the same trend shown in Fig. 6 as the pump amplitude is increased. Interestingly, the amplitude of the oscillations of the Q_{HX} mode and the displacement of the Q_{LZ} mode do increase as the pump frequency is increased, but they vary little as the pump amplitude is increased while keeping the pump frequency fixed.

The very high values of the pump amplitude that we find necessary to break the translation symmetry of $KTaO_3$ are not achievable using currently available laser sources in the midinfrared regime. Thus, our work provides motivation for the development of intense midinfrared lasers. Large electric fields using available midinfrared sources can also be achieved if the sample can be grown inside metallic cavities, and this study should further stimulate the ongoing work to perfect advanced thin-film growth techniques. Furthermore, the high value of the electric field may damage the sample even though the excitation is done for a relatively short duration at frequencies much lower than the band gap of the material. Nevertheless, our study does show that translation symmetry breaking by externally pumping a zone-boundary phonon mode of a material is possible in principle via the mechanism of nonlinear phononics. The physical parameter that limits the efficiency of this phenomenon is the smallness of the coupling between light and two-phonon excitation of the zone-boundary mode. This work motivates the search for a material that exhibits stronger second-order Raman scattering of the zone-boundary phonon than that found in $KTaO_3$.

IV. SUMMARY AND CONCLUSIONS

In summary, we have investigated the possibility of light-induced translation symmetry breaking via nonlinear phononics in $KTaO_3$ by pumping its zone-boundary TO phonon mode. This work was motivated by the previously reported experimental observation of Brillouin zone boundary phonon modes in the Raman spectra of this material due to second-order Raman processes. We calculated the total energy of this material as a function of the highest-frequency TO mode Q_{HX} and degenerate components of the TA mode Q_{LX} and Q_{LZ} from first principles to obtain phonon anharmonicities and phonon-phonon nonlinear couplings. We find that the energy curve of the Q_{LZ} mode softens and develops a double-well shape as the value of the Q_{HX} coordinate is increased, indicating that Q_{LZ} mode becomes unstable when the Q_{HX} mode is pumped with sufficiently intense laser pulses. The coupling between the Q_{HX} mode and light was similarly obtained from first principles by calculating the total energy of this material as a function of the Q_{HX} coordinate and electric field. These were then used to construct coupled equations of motion of the phonon coordinates in the presence of a Gaussian-enveloped single-frequency pump pulse term on the Q_{HX} mode.

We solved the coupled equations of motion for a range of pump frequency and amplitude. We find that $1.8\Omega_{\mathrm{HX}}$ is the smallest pump frequency for which the Q_{LZ} oscillates at a displaced position, and this occurs for a pump amplitude range of 465–520 MV/cm. Since the Q_{LZ} coordinate has a nonzero time-average when it is rectified, this implies that the translation symmetry of this material is broken for this duration. As the pump frequency is increased, the magnitude of the smallest pump amplitude that rectifies the Q_{LZ} mode also increases. These values of pump intensity are at least an order of magnitude larger than that can be produced by currently available midinfrared laser sources. Moreover, the high value of electric field may cause dielectric breakdown of the sample even for a pump pulse of short duration at a frequency much smaller than the band gap of the material. Nonetheless this study shows that light can in principle be used to break the translation symmetry of a material by pumping a phonon mode at the Brillouin zone boundary, opening the door to a new form of materials control via nonlinear phononics.

ACKNOWLEDGMENTS

This work was supported by the Agence Nationale de la Recherche under grant ANR-19-CE30-0004 ELECTROPHONE and GENCI-TGCC under grant A0110913028.

Appendix A: Expression for the Total Energy Surface

The calculated total-energy surface $V(Q_{\rm HX}, Q_{\rm LX}, Q_{\rm LZ})$ was fit with the expression

$$V = \frac{1}{2}\Omega_{\rm LX}^2 Q_{\rm LX}^2 + \frac{1}{2}\Omega_{\rm LZ}^2 Q_{\rm LZ}^2 + \frac{1}{2}\Omega_{\rm HX}^2 Q_{\rm HX}^2 + V^{\rm nh}, \tag{A1}$$

where the nonharmonic part $V^{\rm nh}(Q_{\rm HX}, Q_{\rm LX}, Q_{\rm LZ})$ is given by

$$\begin{aligned} V^{\rm nh} = {} & a_4 Q_{\rm LX}^4 + a_6 Q_{\rm LX}^6 + a_8 Q_{\rm LX}^8 \\ & + b_4 Q_{\rm LZ}^4 + b_6 Q_{\rm LZ}^6 + b_8 Q_{\rm LZ}^8 \\ & + c_4 Q_{\rm HX}^4 + c_6 Q_{\rm HX}^6 + c_8 Q_{\rm HX}^8 \\ & + e_1 Q_{\rm LX}^2 Q_{\rm LZ}^2 + e_2 Q_{\rm LX}^4 Q_{\rm LZ}^2 + e_3 Q_{\rm LX}^2 Q_{\rm LZ}^4 \\ & + e_4 Q_{\rm LX}^6 Q_{\rm LZ}^2 + e_5 Q_{\rm LX}^4 Q_{\rm LZ}^4 + e_6 Q_{\rm LX}^2 Q_{\rm LZ}^6 \\ & + f_0 Q_{\rm HX} Q_{\rm LX} + f_1 Q_{\rm HX}^3 Q_{\rm LX} + f_2 Q_{\rm HX}^2 Q_{\rm LX}^2 \\ & + f_3 Q_{\rm HX} Q_{\rm LX}^3 + f_4 Q_{\rm HX}^5 Q_{\rm LX} + f_5 Q_{\rm HX}^4 Q_{\rm LX}^2 \\ & + f_6 Q_{\rm HX}^3 Q_{\rm LX}^3 + f_7 Q_{\rm HX}^2 Q_{\rm LX}^4 + f_8 Q_{\rm HX} Q_{\rm LX}^5 \\ & + f_9 Q_{\rm HX}^7 Q_{\rm LX} + f_{10} Q_{\rm HX}^6 Q_{\rm LX}^2 + f_{11} Q_{\rm HX}^5 Q_{\rm LX}^3 \\ & + f_{12} Q_{\rm HX}^4 Q_{\rm LX}^4 + f_{13} Q_{\rm HX}^3 Q_{\rm LX}^5 + f_{14} Q_{\rm HX}^2 Q_{\rm LX}^6 \\ & + f_{15} Q_{\rm HX} Q_{\rm LX}^7 \\ & + g_1 Q_{\rm HX}^2 Q_{\rm LZ}^2 + g_2 Q_{\rm HX}^4 Q_{\rm LZ}^2 + g_3 Q_{\rm HX}^2 Q_{\rm LZ}^4 \\ & + g_4 Q_{\rm HX}^6 Q_{\rm LZ}^2 + g_5 Q_{\rm HX}^4 Q_{\rm LZ}^4 + g_6 Q_{\rm HX}^2 Q_{\rm LZ}^6 \\ & + j_1 Q_{\rm HX} Q_{\rm LX} Q_{\rm LZ}^2 + j_2 Q_{\rm HX}^3 Q_{\rm LX} Q_{\rm LZ}^2 \\ & + j_3 Q_{\rm HX}^2 Q_{\rm LX}^2 Q_{\rm LZ}^2 + j_4 Q_{\rm HX} Q_{\rm LX}^3 Q_{\rm LZ}^2 \\ & + j_5 Q_{\rm HX} Q_{\rm LX} Q_{\rm LZ}^4 + j_6 Q_{\rm HX}^5 Q_{\rm LX} Q_{\rm LZ}^2 \\ & + j_7 Q_{\rm HX}^4 Q_{\rm LX}^2 Q_{\rm LZ}^2 + j_8 Q_{\rm HX}^3 Q_{\rm LX}^3 Q_{\rm LZ}^2 \\ & + j_9 Q_{\rm HX}^2 Q_{\rm LX}^4 Q_{\rm LZ}^2 + j_{10} Q_{\rm HX} Q_{\rm LX}^5 Q_{\rm LZ}^2 \\ & + j_{11} Q_{\rm HX}^3 Q_{\rm LX} Q_{\rm LZ}^4 + j_{12} Q_{\rm HX}^2 Q_{\rm LX}^2 Q_{\rm LZ}^4 \\ & + j_{13} Q_{\rm HX} Q_{\rm LX}^3 Q_{\rm LZ}^4 + j_{14} Q_{\rm HX} Q_{\rm LX} Q_{\rm LZ}^6. \end{aligned} \tag{A2}$$

The terms appearing in this expression are those allowed by the symmetry. We found that terms up to the eighth order, with the coefficients smaller than 10^{-7} neglected, suffice to describe calculated total-energy surface. The values of the coefficients appear in Table I.

TABLE I. The coefficients of the harmonic, anharmonic, and nonlinear coupling terms of the polynomial used to fit the calculated total-energy surface $V(Q_{\rm HX}, Q_{\rm LX}, Q_{\rm LZ})$ of $KTaO_3$ as a function of the three X-point phonon coordinates considered in this study. The units are eV $\left(\frac{\text{Å}}{\sqrt{\text{u}}}\right)^{i+j+k}$, where i, j and k are the exponents of the phonon coordinates.

Coefficient	Order	Value	Coefficient	Order	Value
$\Omega^2_{\rm LX}$	$Q^2_{\rm LX}$	0.013636	f_9	$Q^7_{\rm HX}Q_{\rm LX}$	2.92×10^{-5}
$\Omega^2_{\rm LZ}$	$Q^2_{\rm LZ}$	0.013636	f_{10}	$Q^6_{\rm HX}Q^2_{\rm LX}$	3.84×10^{-5}
$\Omega^2_{\rm HX}$	$Q^2_{\rm HX}$	0.955643	f_{11}	$Q^5_{\rm HX}Q^3_{\rm LX}$	2.65×10^{-5}
a_4	$Q^4_{\rm LX}$	7.95×10^{-4}	f_{12}	$Q^4_{\rm HX}Q^4_{\rm LX}$	1.4×10^{-5}
a_6	$Q^6_{\rm LX}$	-7.75×10^{-6}	f_{13}	$Q^3_{\rm HX}Q^5_{\rm LX}$	3.59×10^{-6}
a_8	$Q^8_{\rm LX}$	1.31×10^{-7}	f_{14}	$Q^2_{\rm HX}Q^6_{\rm LX}$	6.7×10^{-7}
b_4	$Q^4_{\rm LZ}$	7.95×10^{-4}	g_1	$Q^2_{\rm HX}Q^2_{\rm LZ}$	-4.789×10^{-4}
b_6	$Q^6_{\rm LZ}$	-7.75×10^{-6}	g_2	$Q^4_{\rm HX}Q^2_{\rm LZ}$	-2.458×10^{-4}
b_8	$Q^8_{\rm LZ}$	1.31×10^{-7}	g_3	$Q^2_{\rm HX}Q^4_{\rm LZ}$	-3.07×10^{-5}
c_4	$Q^4_{\rm HX}$	0.044353	g_4	$Q^6_{\rm HX}Q^2_{\rm LZ}$	-2.01×10^{-6}
c_6	$Q^6_{\rm HX}$	2.649×10^{-4}	g_5	$Q^4_{\rm HX}Q^4_{\rm LZ}$	1.82×10^{-6}
c_8	$Q^8_{\rm HX}$	1.58×10^{-5}	g_6	$Q^2_{\rm HX}Q^6_{\rm LZ}$	3.18×10^{-7}
e_1	$Q^2_{\rm LX}Q^2_{\rm LZ}$	2.796×10^{-4}	j_1	$Q_{\rm HX}Q_{\rm LX}Q^2_{\rm LZ}$	0.001085
e_2	$Q^4_{\rm LX}Q^2_{\rm LZ}$	-1.14×10^{-5}	j_2	$Q^3_{\rm HX}Q_{\rm LX}Q^2_{\rm LZ}$	-2.49×10^{-4}
e_3	$Q^2_{\rm LX}Q^4_{\rm LZ}$	-1.14×10^{-5}	j_3	$Q^2_{\rm HX}Q^2_{\rm LX}Q^2_{\rm LZ}$	-1.233×10^{-4}
e_4	$Q^6_{\rm LX}Q^2_{\rm LZ}$	1.96×10^{-7}	j_4	$Q_{\rm HX}Q^3_{\rm LX}Q^2_{\rm LZ}$	-3.4×10^{-5}
e_5	$Q^4_{\rm LX}Q^4_{\rm LZ}$	2.35×10^{-7}	j_5	$Q_{\rm HX}Q_{\rm LX}Q^4_{\rm LZ}$	-8.7×10^{-5}
e_6	$Q^2_{\rm LX}Q^6_{\rm LZ}$	1.96×10^{-7}	j_6	$Q^5_{\rm HX}Q_{\rm LX}Q^2_{\rm LZ}$	-5.92×10^{-6}
f_0	$Q_{\rm HX}Q_{\rm LX}$	0.0018	j_7	$Q^4_{\rm HX}Q^2_{\rm LX}Q^2_{\rm LZ}$	5.2×10^{-7}
f_1	$Q^3_{\rm HX}Q_{\rm LX}$	0.05605	j_8	$Q^3_{\rm HX}Q^3_{\rm LX}Q^2_{\rm LZ}$	-2.0×10^{-7}
f_2	$Q^2_{\rm HX}Q^2_{\rm LX}$	0.02934	j_9	$Q^2_{\rm HX}Q^4_{\rm LX}Q^2_{\rm LZ}$	-6.8×10^{-7}
f_3	$Q_{\rm HX}Q^3_{\rm LX}$	0.0068	j_{10}	$Q_{\rm HX}Q^5_{\rm LX}Q^2_{\rm LZ}$	1.0×10^{-7}
f_4	$Q^5_{\rm HX}Q_{\rm LX}$	6.03×10^{-4}	j_{11}	$Q^3_{\rm HX}Q_{\rm LX}Q^4_{\rm LZ}$	-2.18×10^{-6}
f_5	$Q^4_{\rm HX}Q^2_{\rm LX}$	1.54×10^{-4}	j_{12}	$Q^2_{\rm HX}Q^2_{\rm LX}Q^4_{\rm LZ}$	-2.94×10^{-6}
f_6	$Q^3_{\rm HX}Q^3_{\rm LX}$	-6.83×10^{-5}	j_{13}	$Q_{\rm HX}Q^3_{\rm LX}Q^4_{\rm LZ}$	-6.3×10^{-7}
f_7	$Q^2_{\rm HX}Q^4_{\rm LX}$	-8.83×10^{-5}	j_{14}	$Q_{\rm HX}Q_{\rm LX}Q^6_{\rm LZ}$	7.4×10^{-6}
f_8	$Q_{\rm HX}Q^5_{\rm LX}$	-1.62×10^{-5}			

[1] R. Mankowsky, M. Först, and A. Cavalleri, Reports on Progress in Physics **79**, 064503 (2016).
[2] P. Salén, M. Basini, S. Bonetti, J. Hebling, M. Krasilnikov, A. Y. Nikitin, G. Shamuilov, Z. Tibai, V. Zhaunerchyk, and V. Goryashko, Physics reports **836**, 1 (2019).
[3] A. Subedi, Comptes Rendus. Physique **22**, 161 (2021).
[4] M. Först, C. Manzoni, S. Kaiser, Y. Tomioka, Y. Tokura, R. Merlin, and A. Cavalleri, Nature Physics **7**, 854 (2011).
[5] A. Subedi, Phys. Rev. B **92**, 214303 (2015).
[6] R. Mankowsky, A. von Hoegen, M. Först, and A. Cavalleri, Phys. Rev. Lett. **118**, 197601 (2017).
[7] M. Henstridge, M. Först, E. Rowe, M. Fechner, and A. Cavalleri, Nature Physics **18**, 457 (2022).
[8] R. Wallis and A. Maradudin, Physical Review B **3**, 2063 (1971).
[9] T. Martin and L. Genzel, physica status solidi (b) **61**, 493 (1974).
[10] A. Subedi, A. Cavalleri, and A. Georges, Phys. Rev. B **89**, 220301 (2014).
[11] A. Subedi, Phys. Rev. B **95**, 134113 (2017).
[12] P. G. Radaelli, Physical Review B **97**, 085145 (2018).
[13] D. M. Juraschek, M. Fechner, and N. A. Spaldin, Physical review letters **118**, 054101 (2017).
[14] M. Fechner and N. A. Spaldin, Physical Review B **94**, 134307 (2016).
[15] M. Gu and J. M. Rondinelli, Scientific reports **6**, 1 (2016).
[16] M. Gu and J. M. Rondinelli, Physical Review B **95**, 024109 (2017).
[17] D. M. Juraschek, M. Fechner, A. V. Balatsky, and N. A. Spaldin, Physical Review Materials **1**, 014401 (2017).
[18] M. Fechner, A. Sukhov, L. Chotorlishvili, C. Kenel, J. Berakdar, and N. Spaldin, Physical review materials **2**, 064401 (2018).
[19] M. Gu and J. M. Rondinelli, Physical Review B **98**, 024102 (2018).
[20] G. Khalsa and N. A. Benedek, npj Quantum Materials **3**, 1 (2018).
[21] J. Park, I. W. Yeu, G. Han, C. S. Hwang, and J.-H. Choi, Scientific Reports **9**, 1 (2019).
[22] D. M. Juraschek, T. Neuman, J. Flick, and P. Narang, Physical Review Research **3**, L032046 (2021).
[23] J. Z. Kaaret, G. Khalsa, and N. A. Benedek, Journal of Physics: Condensed Matter **34**, 035402 (2021).
[24] N. Feng, J. Han, C. Lan, B. Xu, K. Bi, Y. Lin, and C. Nan, Physical Review B **105**, 024304 (2022).
[25] T. F. Nova, A. Cartella, A. Cantaluppi, M. Först, D. Bossini, R. V. Mikhaylovskiy, A. V. Kimel, R. Merlin, and A. Cavalleri, Nature Physics **13**, 132 (2017).
[26] J. Hortensius, D. Afanasiev, A. Sasani, E. Bousquet, and A. Caviglia, npj Quantum Materials **5**, 1 (2020).
[27] M. J. Neugebauer, D. M. Juraschek, M. Savoini, P. Engeler, L. Boie, E. Abreu, N. A. Spaldin, and S. L. Johnson, Physical Review Research **3**, 013126 (2021).
[28] D. Afanasiev, J. Hortensius, B. Ivanov, A. Sasani, E. Bousquet, Y. Blanter, R. Mikhaylovskiy, A. Kimel, and A. Caviglia, Nature materials **20**, 607 (2021).
[29] A. S. Disa, M. Fechner, T. F. Nova, B. Liu, M. Först, D. Prabhakaran, P. G. Radaelli, and A. Cavalleri, Nature Physics **16**, 937 (2020).
[30] A. Melnikov, Y. G. Selivanov, and S. Chekalin, Physical Review B **102**, 224301 (2020).
[31] A. Stupakiewicz, C. Davies, K. Szerenos, D. Afanasiev, K. Rabinovich, A. Boris, A. Caviglia, A. Kimel, and A. Kirilyuk, Nature Physics **17**, 489 (2021).
[32] A. Disa, J. Curtis, M. Fechner, A. Liu, A. von Hoegen, M. Först, T. Nova, P. Narang, A. Maljuk, A. Boris, *et al.*, arXiv preprint arXiv:2111.13622 (2021).
[33] W. G. Nilsen and J. G. Skinner, The Journal of Chemical Physics **47**, 1413 (1967), https://doi.org/10.1063/1.1712096.
[34] A. Cartella, T. F. Nova, M. Fechner, R. Merlin, and A. Cavalleri, Proceedings of the National Academy of Sciences **115**, 12148 (2018), https://www.pnas.org/content/115/48/12148.full.pdf.
[35] P. Giannozzi, O. Baseggio, P. Bonfà, D. Brunato, R. Car, I. Carnimeo, C. Cavazzoni, S. de Gironcoli, P. Delugas, F. Ferrari Ruffino, A. Ferretti, N. Marzari, I. Timrov, A. Urru, and S. Baroni, The Journal of Chemical Physics **152**, 154105 (2020), https://doi.org/10.1063/5.0005082.
[36] K. F. Garrity, J. W. Bennett, K. M. Rabe, and D. Vanderbilt, Computational Materials Science **81**, 446 (2014).
[37] J. P. Perdew, A. Ruzsinszky, G. I. Csonka, O. A. Vydrov, G. E. Scuseria, L. A. Constantin, X. Zhou, and K. Burke, Phys. Rev. Lett. **100**, 136406 (2008).
[38] A. Verma and V. Jindal, Journal of Alloys and Compounds **485**, 514 (2009).
[39] S. Y. Savrasov, D. Y. Savrasov, and O. K. Andersen, Phys. Rev. Lett. **72**, 372 (1994).
[40] D. Bates, S. Kornblith, A. Noack, M. Bouchet-Valat, M. K. Borregaard, A. Arslan, J. M. White, D. Kleinschmidt, G. Lynch, I. Dunning, P. K. Mogensen, S. Lendle, D. Aluthge, pdeffebach, P. José Bayoán Santiago Calderón, B. Born, B. Setzler, C. DuBois, J. Quinn, O. Slámečka, P. Bastide, P. Alday, P. Anthony Blaom, B. König, B. Kamiński, C. Caine, D. Lin, and D. Karrasch, Juliastats/glm.jl: v1.6.0 (2022).
[41] I. Souza, J. Íñiguez, and D. Vanderbilt, Phys. Rev. Lett. **89**, 117602 (2002).
[42] A. Bartels, T. Dekorsy, and H. Kurz, Phys. Rev. Lett. **84**, 2981 (2000).
[43] C. Rackauckas and Q. Nie, The Journal of Open Research Software **5** (2017), exported from https://app.dimensions.ai on 2019/05/05.
[44] M. Frigo and S. G. Johnson, Proceedings of the IEEE **93**, 216 (2005), special issue on "Program Generation, Optimization, and Platform Adaptation".